RESEARCH ARTICLE | JULY 25 2025

Sequential drop impacts onto horizontal fiber arrays

Gene Patrick S. Rible ; Agustin Soto; Regina C. Shome; Andrew K. Dickerson

Physics of Fluids 37, 072128 (2025)
https://doi.org/10.1063/5.0281512
CHORUS

Physics of Fluids ARTICLE pubs.aip.org/aip/pof

Sequential drop impacts onto horizontal fiber arrays

Cite as: Phys. Fluids **37**, 072128 (2025); doi: 10.1063/5.0281512
Submitted: 19 May 2025 · Accepted: 12 June 2025 ·
Published Online: 25 July 2025

Gene Patrick S. Rible,[1] Agustin Soto,[1] Regina C. Shome,[2] and Andrew K. Dickerson[1,a)]

AFFILIATIONS

[1]Department of Mechanical, Aerospace and Biomedical Engineering, University of Tennessee, Knoxville, Tennessee 37996, USA
[2]College of Computing, Georgia Institute of Technology, Atlanta, Georgia 30332, USA

[a)]Author to whom correspondence should be addressed: dickerson@utk.edu

ABSTRACT

We experimentally investigate liquid infiltration into horizontally oriented fiber arrays imposed by sequential drop impacts. Our experimental system is inspired by mammalian fur coats, and our results provide insight to how we expect natural fibers to respond to falling drops and the structure innate to this multiscale covering. Two successive drop impacts are filmed striking three-dimensional-printed fiber arrays with varying densities, surface wettability, and fixed fiber diameter. The penetration depth and the lateral width of drop spreading within fiber layers are functions of drop displacement relative to the liquid already within the array as well as the drop Weber number. Hydrophobic fibers more effectively prevent an increase in penetration depth by the second impacting drop at low impact Weber numbers, whereas hydrophilic fibers ensure lower liquid penetration depth into the array as the Weber number increases. Impact outcomes, such as penetration depth and lateral spreading, are insensitive to impact eccentricity between the first and second drops at high experimental Weber numbers. As expected, denser, staggered fibers reduce infiltration, preventing the entire drop mass from entering the array. Fragmentation of the first drop, which is promoted by hydrophobicity, larger inter-fiber spacing, and higher drop impact velocity, limits increases in lateral spreading and penetration depth of the liquid mass from a subsequent drop.

I. INTRODUCTION

Unlike synthetic methods of rain-avoidance such as umbrellas and raincoats, which create a uniform, sealed waterproof barrier, warmblooded furry mammals have only a porous surface layer to accomplish the same task. The porous nature of the pelt is critical for survival, facilitating both thermal insulation[1,2] and evaporative cooling,[3] allowing the animal to maintain homeostatic body temperature. While the thermoregulatory application of fur and their ability to remove water[4] is well understood, the dynamics of how mammalian fur may effectively mitigate rain infiltration is only beginning to be understood.[5,6]

The physics governing drop infiltration into porous materials such as parallel fibers will be useful for developing biomimetic fur-like materials that are self-cleaning, anti-fouling, and dry quickly.[7–9] Fur can be considered a porous arrangement of organic fiber strands,[10] a slight departure from previous studies, which have considered drop impacts[11–15] and absorption[16,17] into porous inorganic substrates.[18] When drops impact hairy surfaces, capillary action[19–21] causes the drops to disperse throughout the interstices of a porous material until a state of equilibrium is reached.[22,23] Absorption has a positive correlation with porosity,[17,24] contact area,[25] and pore size,[26,27] and a negative correlation with tortuosity.[28] Additionally, a higher impact velocity increases surface spread relative to absorption,[29] and non-cylindrical pore geometries often lead to highly unstable capillary pressure distributions, further restricting capillary flow within a porous medium.[30]

From the standpoint of multiple drop impacts onto natural, porous substances, most existing literature discusses how capillary action causes absorption and film formation into porous stones.[31] Moisture absorption into such a porous substrate depends on the impact velocity of the first set of impacting drops.[31] Thus, capillary imbibition into perforated porous media after multiple drop impacts is well understood. A contrasting substrate, a single fiber, has likewise been the subject of previous studies.[5,32] The experimental system at the center of this study is a superposition of these two contrasting substrates, which more closely mimics the impact of successive drops onto mammalian fur during rainfall.[33] As fur is struck by an impacting drop, the liquid may either penetrate through the laying fibers and/or spread laterally.[5] To understand how mammalian fur coats interact with rain, the present study builds on our single drop study[5] to

investigate how a second drop changes the penetration depth and spread width of the liquid within a three dimensional (3D)-printed fiber array shown in Fig. 1.

A higher fiber packing density and a staggered fiber arrangement reduce the penetration depth of a single drop impacting a horizontally oriented fiber array.[5] The penetration depth of impacting drops appears to plateau to a constant value independent of the Weber number $We = \rho D_0 U^2/\sigma$, where $\rho = 1$ g/ml is the liquid density, D_0 is the equivalent diameter of the drop, U is the impact velocity, and $\sigma = 72.8$ dyn/cm is the surface tension.[5] Hydrophobic fibers resist static penetration, whereas hydrophilic fibers most effectively mitigate dynamic penetration by dissipating kinetic energy through lateral spreading.[5] Our previous results suggest that the ideal fur configuration to remain dry is to carry hydrophilic guard fur to arrest impacting drops and hydrophobic underfur to prevent wicking to the skin.[5] In this work, we explore the mechanisms by which horizontally oriented fibers limit the penetration depth of two sequential drop impacts.

II. EXPERIMENTAL SECTION

A. Fur sample printing and morphology

We simplify the fur system for experimentation by considering only horizontally oriented artificial samples, which are 3D-printed parallel fiber arrays rigidly affixed at both ends shown in Fig. 1(a) as done in a previous study.[5] Resin printer resolution and curing dynamics limit the length and density of the fibers. We can manufacture without the fibers clumping into a unified mass during printing. The fibers are 10 mm long and create a 10 mm × 10 mm array. The fibers are printed with a square cross section of width $l \approx 350\,\mu$m, as shown in Fig. 1(a), but gravity causes the resin to flow in the resin bath into a wedge-like cross section of width $344 \pm 26\,\mu$m (number of samples, $N = 18$) and length $394 \pm 50\,\mu$m ($N = 18$), as shown in Fig. 1(a). The new wedge shape more closely resembles the asymmetrical structure of real mammalian fur[34] and allows us to test the effect of fiber orientation with respect to the impacting drop indicated in Fig. 1(a). We test three orientations of the fiber array with respect to the impacting drop as labeled in Fig. 1(a). While the fiber cross-sectional orientation is an important factor governing the impact dynamics of the first drop,[5] the impact outcome of the second drop is agnostic to fiber cross-sectional orientation.

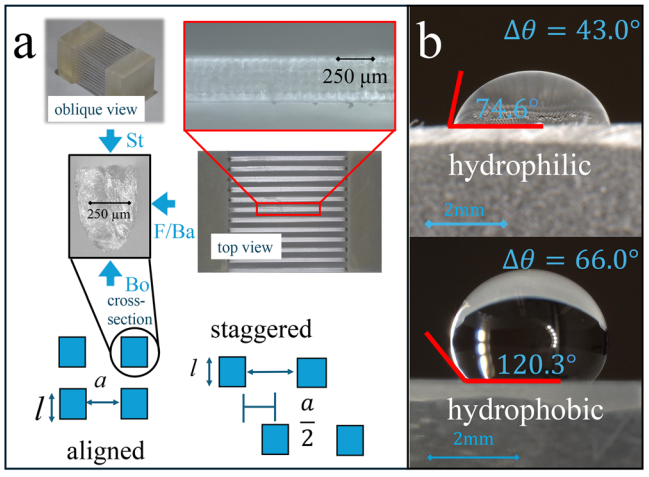

FIG. 1. (a) 3D-printed fiber array in staggered and aligned configurations and in standard (St), front/back (F/Ba), and bottom (Bo) orientations with respect to the impacting drop. (b) Contact angle of water on our hydrophilic and hydrophobic fiber array.

For each packing density, we produce and test two packing configurations, one in which all fibers are aligned in a square grid (aligned) and another in which fibers in an adjacent row are shifted laterally by $a/2$ (staggered), as shown in Fig. 1(a). Fiber packing density is varied by adjusting the inter-fiber spacing a with an average error of 3.8% to form three distinct fiber densities of approximately 50, 100, and 150 strands/cm^2. Our highest fiber array density is greater than that of a Gray Wolf.[35] The intrinsic porosity of the array, derived from fiber width and inter-fiber spacing, can be represented by the dimensionless aspect ratio representing the ratio of empty area to that consumed by fibers on the top row,[5]

$$AR = \frac{a}{l+a}. \tag{1}$$

Solid surfaces have $AR = 0$, single fibers $AR = 1$, and porous media $0 < AR < 1$. A higher AR will intuitively result in greater infiltration but AR neglects the relative size of the impacting drop. The inclusion of drop size is captured in a modified aspect ratio, AR, multiplied by the ratio of fiber-plus-gap unit $\ell + a$ to the drop size,[5,36,37] D_0,

$$AR^* = AR\frac{\ell + a}{D_0} = \frac{a}{D_0} \quad \text{for } \ell + a < D_0. \tag{2}$$

The ability of a drop to penetrate an array is now cursorily described by AR^* as done in our previous studies.[5,6]

Layer-by-layer three-dimensional (3D)-printing produces a tiered structure, as shown in Fig. 1(a). Raw prints have receding, equilibrium, and advancing contact angles of $\theta_r = 46.3 \pm 9.1°$ (number of trials $N = 3$), $\theta_e = 74.6 \pm 6.9°$ ($N = 3$), and $\theta_a = 89.2 \pm 7.0°$ ($N = 3$), respectively. We make an array hydrophobic through vapor phase silanization of the samples using fluorosilane.[38,39] The resulting contact angles are $\theta_r = 62.9 \pm 8.9°$ ($N = 3$), $\theta_e = 120.3 \pm 8.1°$ ($N = 3$), and $\theta_a = 128.8 \pm 7.6°$ ($N = 3$). Sessile drops are pictured on both uncoated and coated samples in Fig. 1(b). The resulting coating is durable against light, temperature of up to 200°C, and pressure sufficient for air-drying.

In our experiments, we allow a drop to impact our fiber array from heights $h = 7, 18, 33,$ and 120 mm resulting in Weber number $We = 1.3 - 92$, as shown in Fig. 2(a). Impact velocity U is calculated by a linear interpolation of temporal drop position from the moment when the drop bottom enters the video frame to when the drop contacts the fibers. The impact Reynolds number is $Re = \rho U D_0/\mu = 480 - 4500$, where $\mu = 1$ cP is the dynamic viscosity; an array Reynolds number $Re^* = \rho U a/\mu = 95 - 2500$[5,40] better characterizes the flow in our fiber arrays. After the first drop has settled within the array, we allow a second drop of the same diameter and height to impact the fiber array. Using image analysis, we calculate the drop spread $\breve{\chi}$ and penetration depth $\breve{d}_p$, nondimensionalized by equivalent drop diameter D_0. D_0 is measured from the binary drop shadow and provided by MATLAB. The uncertainty in our pixel/mm scale conversion is estimated to be less than 4.5%. From measurements, we compute the nondimensionalized change in spread $\Delta\breve{\chi}$ and penetration depth $\Delta\breve{d}_p$ as the difference between their final (second drop)

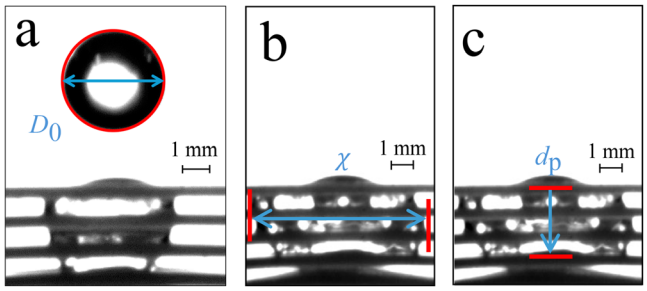

FIG. 2. (a) Tracking the position and measuring the diameter of impacting drop. (b) Tracking the spread of the liquid within the array as a drop impacts an already wetted array. (c) Tracking the penetration depth of the liquid within the array as a drop impacts an already wetted array.

and initial values (first drop), as labeled in Figs. 2(b) and 2(c). We nondimensionalize the temporal coordinate t by the timescale of impact D_0/U, resulting in a dimensionless time τ, where $\tau = 0$ corresponds to the first moment of contact of the impacting drop with the topmost fibers.

A schematic diagram of the experimental setup is depicted in Fig. 3. An electronic syringe pump dispenses drops from a needle. Two high-speed cameras (front view and oblique view) simultaneously capture the drop impact, illuminated by back and side lights. Videos from the front view camera are used for experimental measurements, whereas the videos from the oblique view camera are used to ensure impact locations are within the array bounds.

III. RESULTS AND DISCUSSION

We perform 432 sequential drop impact trials onto horizontal fiber arrays, measuring the change in penetration depth and liquid spreading width. 216 trials were performed with aligned arrays and 216 with staggered arrays. We present data for aligned arrays in the manuscript and include staggered array data in the online supplement. Fiber alignment is relevant only in discussion of supersurface retention (Sec. III A). More broadly, array density, wettability, and drop impact velocity and location collectively influence drop impact behavior.

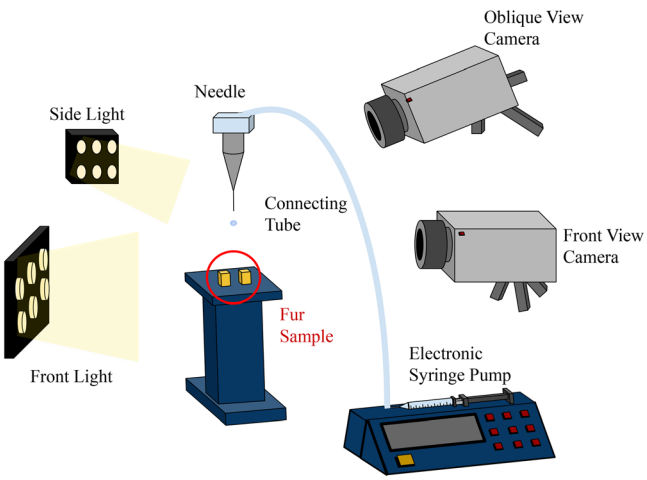

FIG. 3. Experimental setup. A front view camera measures penetration depth and lateral spreading while an oblique view camera ensures the drop's impact within array bounds.

A. What promotes supersurface drop retention atop the fiber array?

We categorize the liquid state after the first and the second drop according to the degree of supersurface retention and fragmentation, as shown in Fig. 4. We plot the aligned fiber impacts classified according to the initial degree of supersurface retention across the modified aspect ratio AR^* of the fiber arrays and the Weber number We in Figs. 5(a) and 5(b). The penetration depth of the drop into the array nondimensionalized by the D_0, $\breve{d}_p$, is given by the color gradient. The resulting supersurface retention after the impact of the second drop is shown in Figs. 5(c) and 5(d). Staggered fibers produce very similar behaviors, which are not shown for the sake of brevity but included in Fig. S1. Brighter colors correspond to higher penetration depths, quantized according to the number of fiber rows penetrated. The final state of the second drop is very likely equivalent to the post-impact state of the first drop, summarized in Figs. 6(a) and 6(b), which include all our experiments. Thus, the state of the initial liquid within the array predetermines the state of subsequent impacting drops. Hydrophobicity and density of fiber arrays promote supersurface retention. When $We < 10$ and $AR^* < 0.35$, all of the drop masses are retained on the top fiber row of hydrophobic arrays. At higher We, partial retention (●) is more likely when the fibers are sparser, $AR^* > 0.35$, regardless of wettability. Total (◇) and partial (●) supersurface retention can be combined into one classification to compare any supersurface retention vs those impacts that exhibit none. With this scheme, staggered fibers marginally improve total supersurface retention (30% of impacts) than their aligned counterparts (23% of impacts), as seen by comparing Figs. 6(c) and 6(d) with Figs. 6(e) and 6(f).

B. What promotes double-drop spreading along fiber axes?

While first and second drops are always released from the same location, we observe stochastic variation in their impact location, a variation that increases with release height. Intuitively, lateral displacement of the impact axes between the first and second drops δ would promote an increase in the final lateral spread of liquid mass within the array $\Delta\breve{\chi}$. However, the outcome of $\Delta\chi$ is more nuanced and dependent on We. We summarize our observations in Table I. We provide image sequences corresponding to each case in Table I, as shown in Fig. 7 (Multimedia view). At our lower experimental We values, $\Delta\breve{\chi} > 0$ for aligned and misaligned second drops as photographically depicted in Figs. 7(a) and 7(b). Drops do not fragment at low We, and so the liquid mass in the array grows by the addition of the second drop. At higher We, fragmentation is promoted, and drop alignment $\delta \approx 0$ results in $\Delta\breve{\chi} > 0$, which is true for both the non-fragmented case shown in Fig. 7(c) and the fragmented case shown in Fig. 7(d). However, when $\delta > 0$ and the initial liquid in the array is fragmented, the impacting drop momentarily fills voids left by the first drop by adhering to the smaller fragments trailing the now static first drop mass. The penetrating second drop is pulled toward the existing liquid

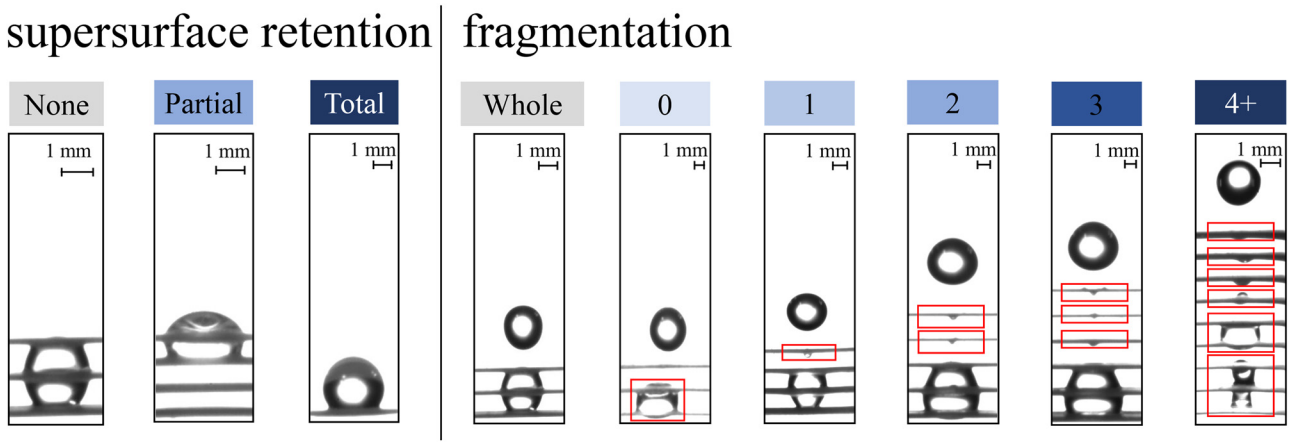

FIG. 4. Classifications of the degree of supersurface retention and fragmentation of liquid within the array. "Whole" when the liquid within the fiber array is not fragmented and occupies the topmost inter-fiber space; (0) the liquid is not fragmented, but the topmost inter-fiber space is not occupied; (1) a single fragment is visible above the main liquid body within the array; (2) two fragments are visible; (3) three fragments are visible; (4+) the liquid within the array has split into four or more visibly separate bodies. Liquid within the array in each panel consists of the first impacting drop.

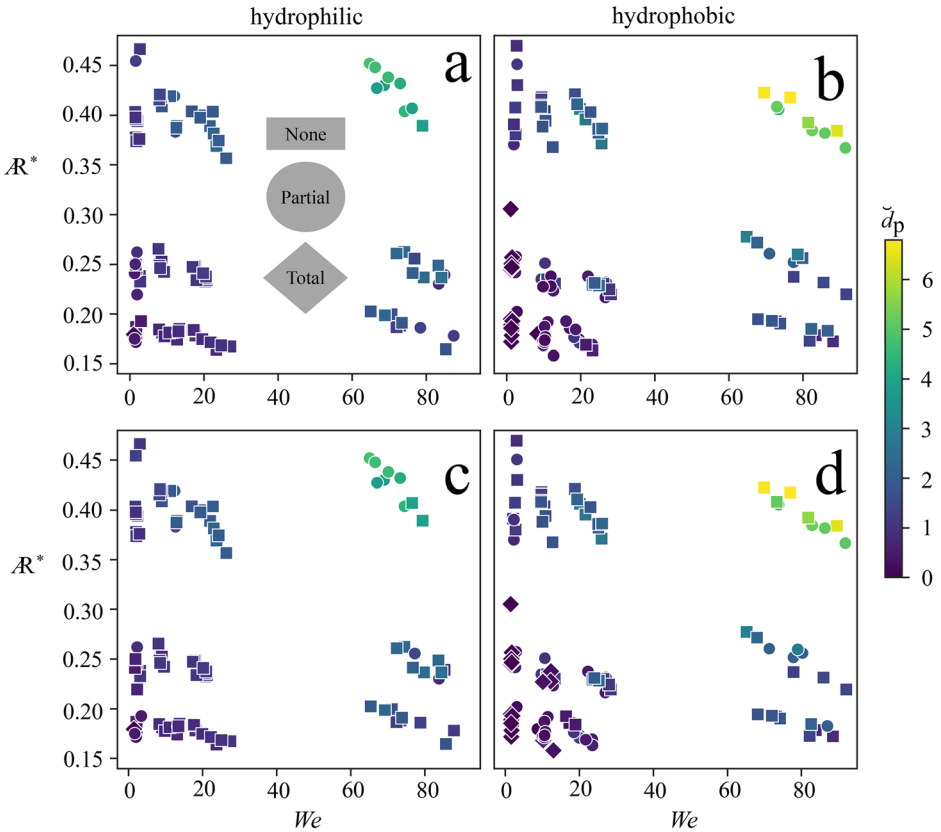

FIG. 5. Aligned fiber impacts classified according to the degree of supersurface retention and plotted across the modified aspect ratio $\mathcal{R}^*$ and Weber number *We*. Brighter colors correspond to higher penetration depths, refer to Fig. 4. (a) and (b) Impact classifications after the first drop. (c) and (d) Impact classifications after the second drop.

fragments within the array, resulting in a nearly zero $\Delta\breve{\chi}$, as shown in Fig. 7(e), or sometimes, a reduction in χ, as shown in Fig. 8(a) (Multimedia view). In hydrophobic fibers, a reduction in χ is possible for fragmented drops, whereas a reduction in d_p is possible for non-fragmented drops, as shown in Fig. 8(b) (Multimedia view).

We present a more global view of how fragmentation influences $\Delta\breve{\chi}$ across δ in Figs. 9(a) and 9(b). A figure corresponding to Fig. 9 for staggered fibers is shown in Fig. S2. Color-coded data points show that as a drop fragments into more parcels, $\Delta\breve{\chi}$ is kept low, even for relatively extreme δ values, an observation that is more pronounced for

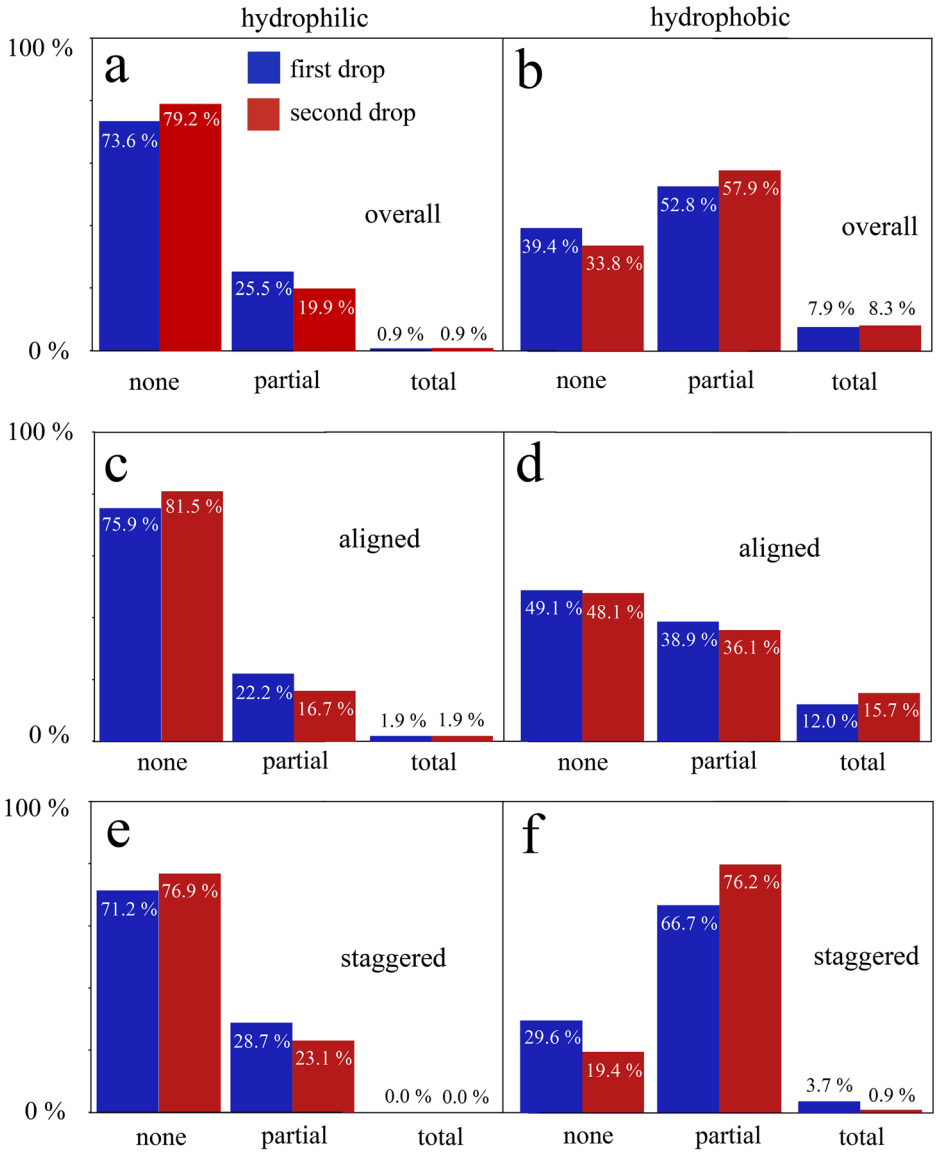

FIG. 6. Percentage of infiltration types after the first drop (blue) and second drop (red) for (a) and (b) combined experiments, (c) and (d) aligned fibers, and (e) and (f) staggered fibers. Refer to Fig. 4.

hydrophilic fibers. The observation of low $\Delta\breve{\chi}$ imposed by fragmentation is a result of the void filling and parcel coalescence shown in Fig. 7(e). We plot $\Delta\breve{\chi}$ vs *We* in Figs. 9(c) and 9(d). The change in spread $\Delta\breve{\chi}$ is independent of *We*, and drops are more likely to fragment at high *We*, as expected. In hydrophobic fibers [Figs. 9(b) and 9(d)], the effect of fragmentation is less pronounced, and $\Delta\breve{\chi} < 0$ occurs more likely at high *We*.

TABLE I. Change of spread and penetration as a function of second drop displacement and Weber number. An upward arrow ↑ indicates an increase, a hyphen (-) indicates no change, and a downward arrow ↓ indicates a decrease.

We	δ	$\Delta\breve{\chi}$	$\Delta\breve{d}_p$
$\approx 1-30$	≈ 0	↑	↑
$\approx 1-30$	>0	↑ (not fragmented) - or ↓ (fragmented)	⋯
$\approx 60-100$	≈ 0	↑	⋯
$\approx 60-100$	>0	⋯	⋯

Second drop displacement perpendicular to both impact and fiber axes, out-of-plane of the front camera, reduces spreading along the fiber axes by virtue of conservation of mass. In contrast, δ does not affect the trans-fiber spreading because of the fiber-imposed restriction on out-of-plane motion.[5]

C. What promotes double-drop penetration into the array?

A greater lateral distribution of liquid mass ensures that penetration depth is unlikely to increase when $\delta > 0$ (Fig. 7 and Table I), as shown in Figs. 10(a) and 10(b). A figure corresponding to Fig. 7 for staggered fibers is shown in Fig. S3. Second drop displacement

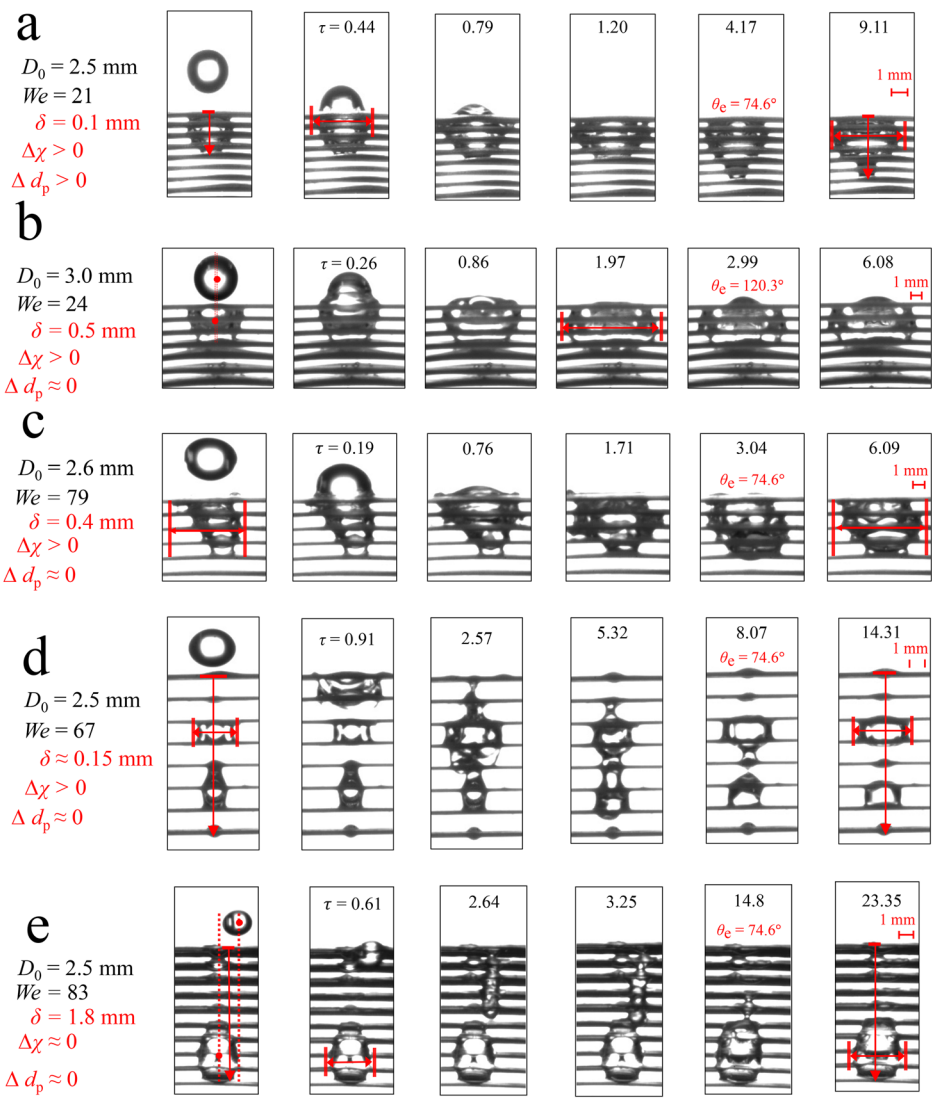

FIG. 7. Displacement of drop relative to liquid within the array inhibits increase in liquid spread and penetration depth. (a) $\delta \approx 0$ at $We \approx 20$. (b) $\delta > 0$ at $We \approx 20$. (c) $\delta \approx 0$ at $We \approx 60 - 80$ without fragmentation. (d) $\delta \approx 0$ at $We \approx 60 - 80$ with 4+ fragmentation. (e) $\delta > 0$ at $We \approx 60 - 80$. Multimedia available online.

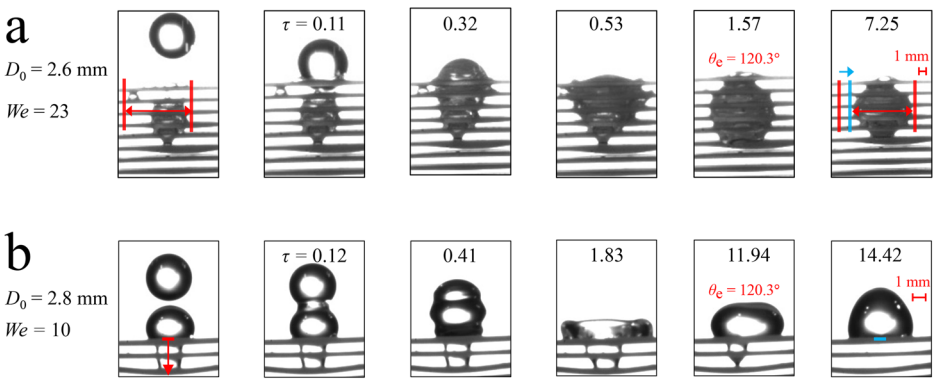

FIG. 8. (a) Hydrophilic fibers allow for $\Delta\tilde{\chi} < 0$ at high *We*. (b) Hydrophobic fibers allow for $\Delta\tilde{d}_p < 0$ at low *We*. Multimedia available online.

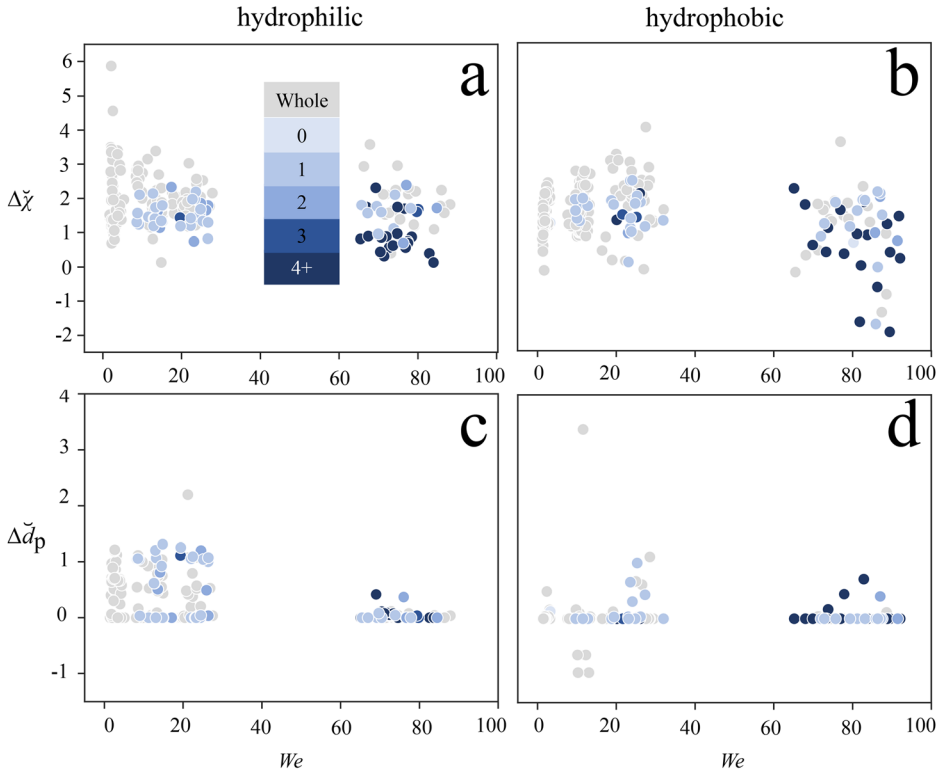

FIG. 9. Change in spreading of liquid mass within the aligned array imposed by the second drop. (a) and (b) Dimensionless change in spread vs the dimensionless horizontal displacement of the second drop relative to the first drop. (c) and (d) Dimensionless change in spread vs the impact Weber number. Colors indicate the degree of fragmentation, refer to Fig. 4. Plots on the left column correspond to hydrophilic fiber arrays, and those on the right column correspond to hydrophobic fiber arrays.

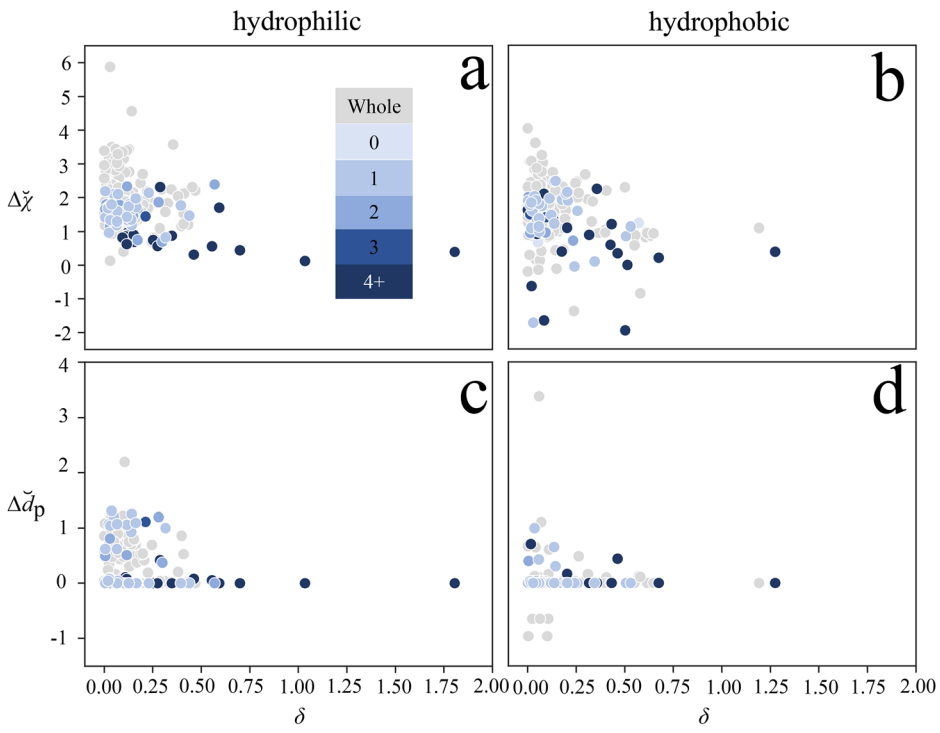

FIG. 10. Change of penetration depth within the aligned array imposed by the second drop. (a) and (b) Dimensionless change in penetration depth vs the dimensionless horizontal displacement of the second drop relative to the first drop. (c) and (d) Dimensionless change in penetration depth vs impact Weber number. Colors indicate degree of fragmentation; refer to Fig. 4. Plots on the left column correspond to hydrophilic fiber arrays, and those on the right column correspond to hydrophobic fiber arrays.

perpendicular to both impact and fiber axes, not strictly observable with our experimental setup, reduces penetration depth by virtue of conservation of mass—the fiber configuration limits out-of-plane motion.[5,6] Second drops producing $\delta \approx 0$ push liquid beyond the existing static mass much like the expulsion of balls from Newton's cradle, an expulsion that is nonintuitively less dramatic at high *We*. At high *We*, the first drop fragments as shown in Figs. 7(d) and 7(e). The second impacting drop also fragments, and its fragments coalesce with the parcels of liquid waiting in the array. The result is almost no change in the penetration depth. Thus, an increase in penetration depth is only promoted when $\delta \approx 0$, and the liquid in the array is not fragmented. Since hydrophilic fiber arrays limit the penetration depth of the first drop compared with their hydrophobic counterparts,[5] then, by extension, hydrophilic fibers limit the penetration of successive drops. Such a property is important for a fibrous, fur-like, raincoat in heavy rainfall.

The change in penetration depth is independent of *We* as shown in Figs. 10(c) and 10(d). At $We \gtrsim 60$, there is almost zero change in penetration. At low *We*, hydrophobic fibers allow for a reduction of penetration depth through a combination of rebound and surface tension, pulling up the liquid that is already within the array as shown in Fig. 8(b).

The antithesis of array penetration is drop rebound, an easier metric to observe for arrays that provide little to no visual access. The degree of rebound, though not strictly quantified here, corresponds to a range of rebound behaviors. We classify rebound types according to the shapes they produce and their qualitative height, as shown in Fig. 11 (Multimedia view). In cases where multiple sequential rebounds occur after impact, only the first rebound is classified.

Higher *We* and AR^* enhance drop penetration and fragmentation while reducing rebound, as mentioned in our previous work[5] so that an increase in *We* may be compensated by a decrease in AR^* and vice versa. The product of *We* and AR^* is, thus, a useful metric by which to describe drop fragmentation, penetration, and rebound. A similar approach has been done in other investigations.[6,36,37] A plot of AR^*We color-coded by rebound type is shown in Fig. 12(a). Rebound is promoted in hydrophobic fibers with the jet-to-bulb transition in the rebound shape shown in Fig. 11 ("jet-bulb") occurring at low AR^*We. The jet-like rebound, with a sharper rebounding jet that does not produce a round bulb, appears in both hydrophilic and hydrophobic fibers. In a previous study,[5] we found that rebound is promoted by higher fiber density and lower impact speed for a single impacting drop, an observation that remains true for a second, sequential drop. Rebound and other impact behavior of the second drop are influenced by the distribution of the liquid that is already within the array; the second drop mimics the rebound behavior of the first, as discussed earlier. At low *We*, liquid mass retention atop the array is prominent, promoting jet-like and jet-bulb rebound. The more the drop rebounds, the less it penetrates, as shown in Fig. 12(b).

At low *We*, rebounding drops can pull the liquid within the fiber upward as the drop rebounds in hydrophobic fibers, resulting in $\Delta\tilde{d}_p < 0$, as shown in Fig. 12(c) and as pictured in Fig. 8(b). Such a reduction does not occur in our hydrophilic fibers where the contact lines are pinned.

IV. CONCLUSIONS

In this study, we take the canonical topic of a single impacting drop further by studying the impact outcome of a second drop impacting an already wet fibrous array. The final state of a second drop impacting onto a fiber array is predetermined by the state of the liquid within the array. The change in penetration depth and spread of the liquid within the array occurred when a second drop impacts is poorly correlated with *We*. Hydrophobicity promotes supersurface retention and enables a decrease in spread at high *We* and a decrease in penetration depth at low *We*. In contrast, hydrophilic fibers limit the penetration depth of successive drops at high *We*. Such characteristics explain why it would benefit mammals or engineered systems coated with fur-like structures to carry a hydrophobic underfur and

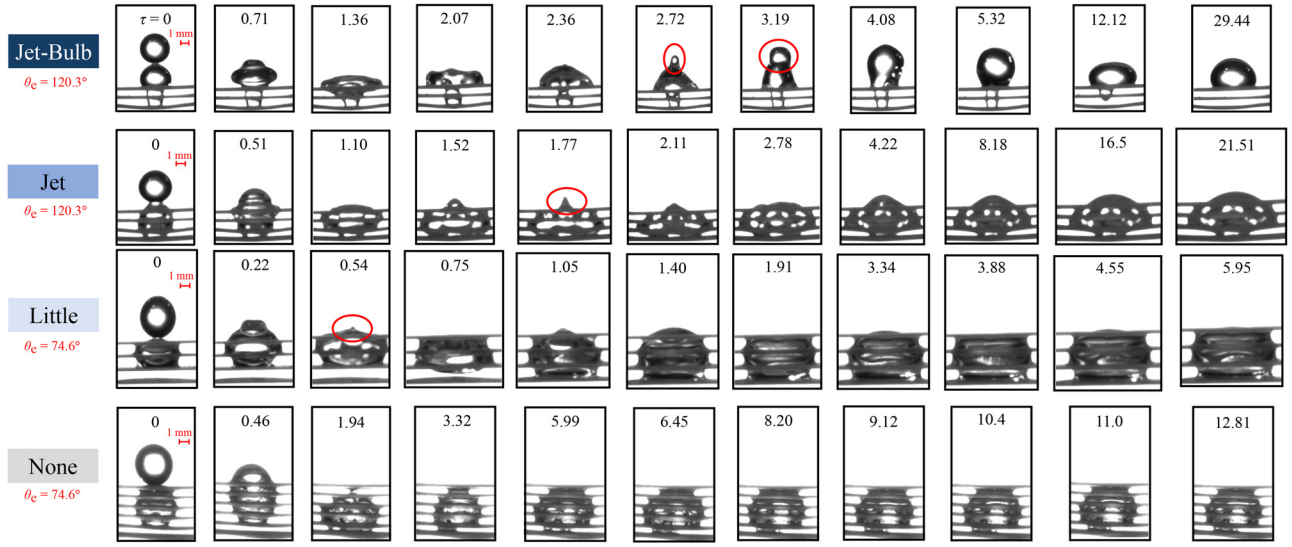

FIG. 11. Rebound classifications. Impacts are classified according to the shape of the rebounding jet. Each frame is timestamped by dimensionless time τ. Multimedia available online.

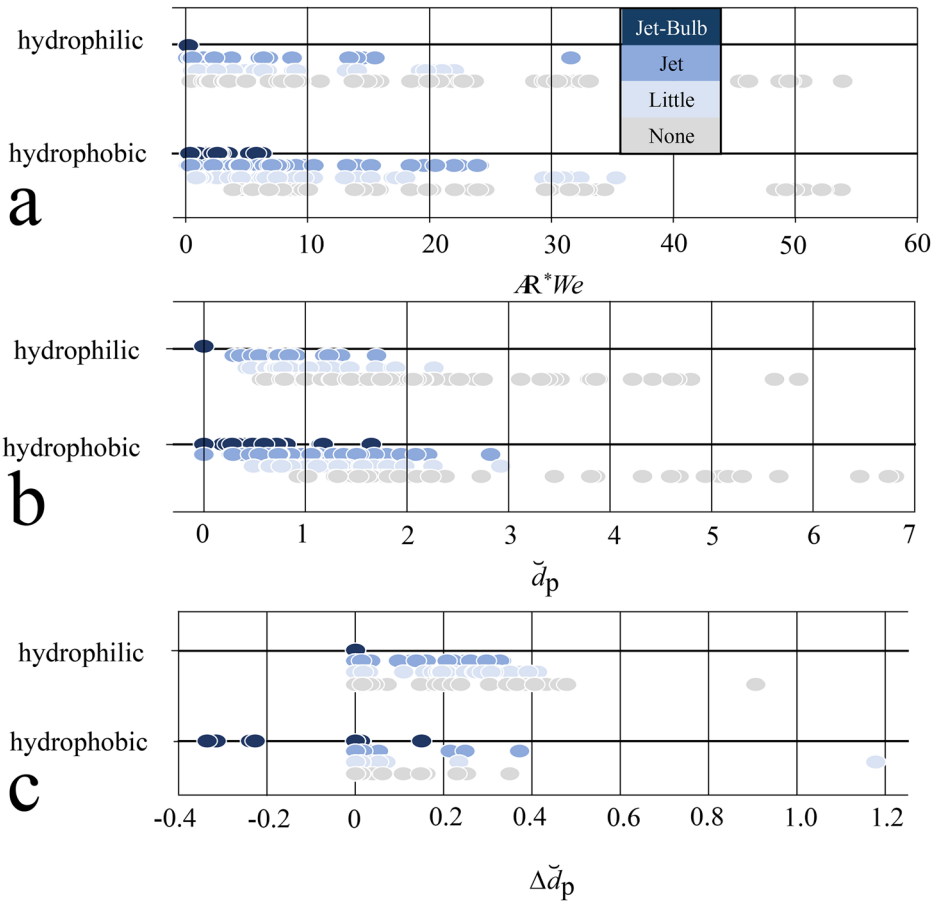

FIG. 12. Rebound classifications of the second drop plotted according to (a) $\mathcal{A}R^*We$, (b) $\breve{d}_p$, and (c) $\Delta\breve{d}_p$. Includes data from aligned and staggered fiber arrays.

hydrophilic guard fur, allowing water-proofing even during a heavy rainfall.

SUPPLEMENTARY MATERIAL

See the supplementary material for three figures showing data corresponding to drop impact onto staggered fibers.

ACKNOWLEDGMENTS

This research was partially funded by the National Science Foundation (CMMI 1825801 and CBET 2205558). We thank Isabelle Garrett, an undergraduate research assistant at the Fluids and Structures Laboratory, for editing the image sequences and supplemental videos.

AUTHOR DECLARATIONS

Conflict of Interest

The authors have no conflicts to disclose.

Author Contributions

Gene Patrick S. Rible: Conceptualization (lead); Data curation (equal); Formal analysis (equal); Investigation (lead); Methodology (lead); Project administration (lead); Software (supporting); Supervision (lead); Validation (supporting); Visualization (supporting); Writing – original draft (equal); Writing – review & editing (equal). **Agustin Soto:** Data curation (equal); Formal analysis (supporting); Investigation (supporting); Methodology (equal); Project administration (supporting); Software (lead); Validation (supporting); Visualization (supporting); Writing – original draft (supporting). **Regina C. Shome:** Formal analysis (supporting); Investigation (equal); Software (supporting); Validation (lead); Visualization (lead); Writing – original draft (equal); Writing – review & editing (supporting). **Andrew K. Dickerson:** Data curation (equal); Formal analysis (equal); Funding acquisition (lead); Investigation (supporting); Methodology (supporting); Resources (lead); Supervision (supporting); Writing – review & editing (equal).

DATA AVAILABILITY

The data that support the findings of this study are available from the corresponding author upon reasonable request.

REFERENCES

[1]N. Erdsack, G. Dehnhardt, and W. Hanke, "Coping with heat: Function of the natal coat of cape fur seal (arctocephalus pusillus pusillus) pups in maintaining core body temperature," PLoS One **8**, e72081 (2013).
[2]C. Chesney, "The microclimate of the canine coat: The effects of heating on coat and skin temperature and relative humidity," Vet. Dermatol. **8**, 183–190 (1997).

[3]K. G. Gebremedhin and B. Wu, "Sensible and latent heat losses from wet-skin surface and fur layer," in *2001 ASAE Annual Meeting*. American Society of Agricultural and Biological Engineers (ASAE, 1998), p. 1.
[4]A. K. Dickerson, Z. G. Mills, and D. L. Hu, "Wet mammals shake at tuned frequencies to dry," J. R. Soc. Interface **9**, 3208–3218 (2012).
[5]G. P. S. Rible, M. A. Spinazzola III, R. E. Jones III, R. U. Constantin, W. Wang, and A. K. Dickerson, "Dynamic drop penetration of horizontally oriented fiber arrays," Langmuir **40**, 13339 (2024).
[6]G. P. S. Rible, V. Chakpuang, A. D. Holihan, H. P. Sebek, H. H. Osman, K. R. Brown, W. Wang, and A. K. Dickerson, "Dynamic drop penetration of vertically oriented fiber arrays," Phys. Fluids **37**, 022108 (2025).
[7]B. Bhushan, "Biomimetics: Lessons from nature—An overview," Philos. Trans. R. Soc. A **367**, 1445–1486 (2009).
[8]S. Usenyuk-Kravchuk, N. Garin, A. Trofimenko, and D. Kukanov, "Arctic design: Revisiting traditional fur clothing within the daily routine of reindeer nomads," Heliyon **6**, e03355 (2020).
[9]V. Kapsali, "Biomimetic principles for design of water repellent surfaces," in *Waterproof and Water Repellent Textiles and Clothing* (Elsevier, 2018), pp. 121–135.
[10]T. M. P. Hardy and J. I. Hardy, "Types of fur fibers," J. Heredity **33**, 191–199 (1942).
[11]N. C. Reis, Jr., R. F. Griffiths, and J. M. Santos, "Numerical simulation of the impact of liquid droplets on porous surfaces," J. Comput. Phys. **198**, 747–770 (2004).
[12]C. Josserand and S. T. Thoroddsen, "Drop impact on a solid surface," Annu. Rev. Fluid Mech. **48**, 365–391 (2016).
[13]A. N. Lembach, I. Roisman, and C. Tropea, "Drop impact on porous media," in *Proceedings of the DIPSI Workshop*, Bergamo, Italy (Università degli Studi di Bergamo, 2011), pp. 28–32.
[14]P. Zhao, G. K. Hargrave, H. K. Versteeg, C. P. Garner, B. A. Reid, E. Long, and H. Zhao, "The dynamics of droplet impact on a heated porous surface," Chem. Eng. Sci. **190**, 232–247 (2018).
[15]M. Choi, G. Son, and W. Shim, "Numerical simulation of droplet impact and evaporation on a porous surface," Int. Commun. Heat Mass Transfer **80**, 18–29 (2017).
[16]M. Choi, G. Son, and W. Shim, "A level-set method for droplet impact and penetration into a porous medium," Comput. Fluids **145**, 153–166 (2017).
[17]J. B. Lee, "Droplet dynamics on non-porous and porous media: Impact, spreading and absorption," Ph.D. thesis (ETH Zurich, 2015).
[18]R. Rioboo, M. Voué, A. Vaillant, and J. De Coninck, "Drop impact on porous superhydrophobic polymer surfaces," Langmuir **24**, 14074–14077 (2008).
[19]F. Bashforth and J. C. Adams, *An Attempt to Test the Theories of Capillary Action by Comparing the Theoretical and Measured Forms of Drops of Fluid* (University Press, 1883).
[20]R. Masoodi and K. Pillai, "A general formula for capillary suction-pressure in porous media," J. Porous Media **15**, 775 (2012).
[21]A. Wysocki and H. Rieger, "Capillary action in scalar active matter," Phys. Rev. Lett. **124**, 048001 (2020).
[22]L. Hocking and A. Rivers, "The spreading of a drop by capillary action," J. Fluid Mech. **121**, 425–442 (1982).
[23]N. R. Morrow, "Physics and thermodynamics of capillary action in porous media," Ind. Eng. Chem. **62**, 32–56 (1970).
[24]S. Hosseini, "Droplet impact and penetration onto structured pore network geometries," Ph.D. thesis (University of Toronto, 2015).
[25]R. Chebbi, "Absorption and spreading of a liquid droplet over a thick porous substrate," ACS Omega **6**, 4649–4655 (2021).
[26]J. Lee, D. Derome, and J. Carmeliet, "Drop impact on natural porous stones," J. Colloid Interface Sci. **469**, 147–156 (2016).
[27]H. Tan, "Absorption of picoliter droplets by thin porous substrates," AlChE J. **63**, 1690–1703 (2017).
[28]M. Matyka, "Pushing droplet through a porous medium," Transp. Porous Media **144**, 55–68 (2022).
[29]P. Alam, M. Toivakka, K. Backfolk, and P. Sirviö, "Impact spreading and absorption of Newtonian droplets on topographically irregular porous materials," Chem. Eng. Sci. **62**, 3142–3158 (2007).
[30]Z. Sun, "Capillary phenomena in porous media: Pore and grain scale studies," Ph.D. thesis (Georgia Institute of Technology, 2018).
[31]D. Derome, S. Carl, P. Vontobel, and J. Carmeliet, "Adsorption and film forming of train of water droplets impacting porous stones," in *Proceedings of the 7th International Building Physics Conference* (International Building Physics Association, 2018), pp. 73–78.
[32]J. Comtet, B. Keshavarz, and J. W. Bush, "Drop impact and capture on a thin flexible fiber," Soft Matter **12**, 149–156 (2016).
[33]K. Sarkar and B. Bhattacharjee, "Modeling of tropical rainfall exposure for the study of moisture penetration in porous building materials," J. Hydrol. Eng. **22**, 04017017 (2017).
[34]M. Krsmanovic, H. Ali, D. Biswas, R. Ghosh, and A. K. Dickerson, "Fouling of mammalian hair fibres exposed to a titanium dioxide colloidal suspension," J. R. Soc. Interface **19**, 20210904 (2022).
[35]M. W. Kulbaba, "Investigating epizoochorous adaptations to mammalian furs," Ph.D. thesis (Department of Biology, University of Winnipeg, 2004).
[36]G. Zhang, M. A. Quetzeri-Santiago, C. A. Stone, L. Botto, and J. R. Castrejón-Pita, "Droplet impact dynamics on textiles," Soft Matter **14**, 8182–8190 (2018).
[37]D. J. Bouchard, "Droplet impact, infiltration, and boiling in pores and porous media," Ph.D. thesis (University of Toronto, 2021).
[38]W. Wang, X. Du, H. Vahabi, S. Zhao, Y. Yin, A. K. Kota, and T. Tong, "Trade-off in membrane distillation with monolithic omniphobic membranes," Nat. Commun. **10**, 3220 (2019).
[39]W. Wang, J. Salazar, H. Vahabi, A. Joshi-Imre, W. E. Voit, and A. K. Kota, "Metamorphic superomniphobic surfaces," Adv. Mater. **29**, 1700295 (2017).
[40]P. J. Pritchard and J. W. Mitchell, *Fox and McDonald's Introduction to Fluid Mechanics* (John Wiley & Sons, 2016).